Application of the perfectly matched layer (PML) absorbing boundary condition to elastic wave propagation

Frank D. Hastings,[a] John B. Schneider, and Shira L. Broschat
School of Electrical Engineering and Computer Science, Washington State University, Pullman, Washington 99164-2752

(Received 14 June 1995; accepted for publication 13 November 1995)

A method is presented for application of the perfectly matched layer (PML) absorbing boundary condition (ABC) to the *P-SV* velocity–stress finite-difference method. The PML consists of a nonphysical material, containing both passive loss and dependent sources, that provides ''active'' absorption of fields. It has been used in electromagnetic applications where it has provided excellent results for a wide range of angles and frequencies. In this work, numerical simulations are used to compare the PML and an ''optimal'' second-order elastic ABC [Peng and Toksöz, J. Acoust. Soc. Am. **95**, 733–745 (1994)]. Reflection factors are used to compare angular performance for continuous wave illumination; snapshots of potentials are used to compare performance for broadband illumination. These comparisons clearly demonstrate the superiority of the PML formulation. Within the PML there is a 60% increase in the number of unknowns per grid cell relative to the velocity–stress formulation. However, the high quality of the PML ABC allows the use of a smaller grid, which can result in a lower overall computational cost.

PACS numbers: 43.30.Ma, 43.30.Ky, 43.20.Gp, 43.20.Jr [JHM]

INTRODUCTION

Absorbing boundary conditions (ABCs) are widely used in numerical simulations of unbounded problems. They are enforced at the edges of a computational domain to absorb outgoing waves and thereby model an unbounded region. A number of ABCs have been introduced for use in finite-difference modeling of elastic wave propagation. The ABCs of both Levander[1] and Cerjan *et al.*[2] introduce a lossy material layer to attenuate fields near the computational boundary. These have been used in a number of applications.[3–7] An approach based on a paraxial approximation of the elastic wave equation was introduced by Clayton and Engquist.[8] Several formulations generalizing this method are available in the literature, including Higdon,[9–11] Long and Liow,[12] and Reynolds.[13] Higdon,[9] Liao *et al.*,[14] and Peng and Toksöz[15] have constructed ABCs for which fields on the boundary of the computational domain are extrapolated from interior fields. Randall[16] has presented an ABC which transforms velocities to potentials. This permits the use of any scalar ABC in the elastic problem. Randall used Lindman's ABC (Ref. 17) which is a scalar ABC based on the one-way wave equation.

Since ABCs absorb waves imperfectly, artificial reflections occur at the edges of the computational domain. These reflections can limit the dynamic range or degrade the accuracy of results; thus, it is desirable to obtain the best possible ABC performance. Ideally, an ABC should perform well, independent of frequency and incident angle, while remaining computationally tractable. However, in practice, ABC performance degrades beyond a specific range of angles and frequencies. In this paper, an ABC is presented that performs well over a broader range of angles and frequencies than those previously presented. Specifically, Randall's transformation is used in conjunction with the recently introduced perfectly matched layer (PML) ABC developed by Berenger.[18] It is considered to be the best material ABC currently available because of its excellent absorption over a wide range of angles and its insensitivity to frequency.[19] The PML ABC has been used extensively in electromagnetic modeling and has been further developed in other recent papers. Chew and Weedon[20] present a derivation based on stretched coordinates,[21] which reproduces the equations given in Ref. 18. Mittra and Pekel[22] discuss several aspects of the PML technique, provide an alternate form of the equations, and show that the PML is an anisotropic active medium containing dependent sources. Reuter *et al.*[23] show that the PML can absorb energy over a broad frequency spectrum. In acoustics, a fluid medium PML formulation has recently been presented by Maloney and Cummings.[24]

In this paper, we consider a 2-D elastic medium PML formulation. We describe the transformation process, present the equations used in the lossy layer, and give numerical results using test simulations. The ''optimal'' ABC of Peng and Toksöz[15] is compared with the PML in two performance tests. First, the ABCs are illuminated by a continuous wave (cw) cylindrical wave, and reflection factors are computed that measure the angular performance of each ABC. Second, a test geometry is illuminated with a Ricker wavelet to examine broadband performance of each ABC. Both tests show that the PML performs better than the ''optimal'' ABC for absorption of both *P*- and *S*-wave energy.

I. IMPLEMENTATION

Figure 1 shows the geometry of a 2-D, finite-difference grid with a PML. In the interior, the *P-SV* velocity–stress

[a]Electronic mail: fhasting@eecs.wsu.edu

 0001-4966/96/100(5)/3061/9/$10.00

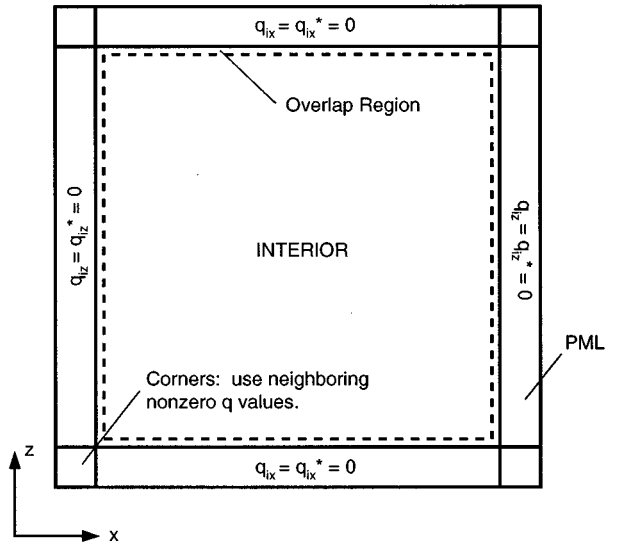

FIG. 1. Computational grid with PML absorbing boundary. Interior fields are computed using the velocity–stress formulation, and PML fields are computed using potentials. In the overlap region the waves are transformed back and forth between velocities and potentials.

finite-difference formulation is applied,[25] and in the PML the waves are propagated separately as shear and compressional potentials. The velocity-potential conversions take place in a one grid-cell wide overlap region. Square grid cells of area Δ^2 are assumed. Figure 2 shows a section of the overlap region for the left edge of the interior. Within the PML, two offset grids are overlayed with the result that two field values occur at each half-grid space (i.e., $\Delta/2$). In the overlap region, both the PML potentials and the standard velocity–stress components are computed. The values with boxed labels are used to convert back and forth between velocities and potentials. Some fields in this region are omitted to indicate that they are unnecessary for the finite-difference computations. The outer edge of the PML (not shown) can be terminated by either a Dirichlet or a Neumann boundary condition.

Velocity is related to potential by[16]

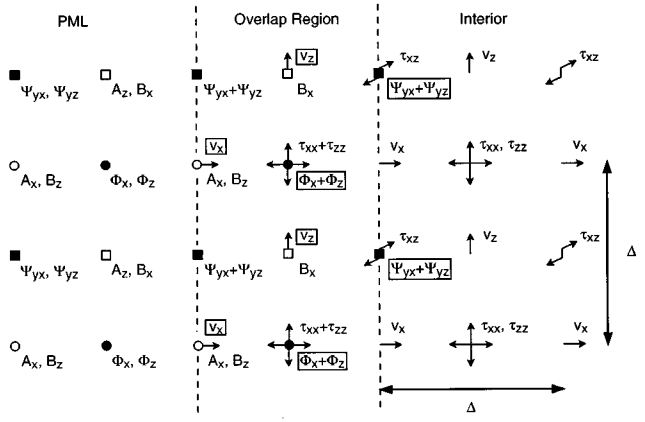

FIG. 2. Left edge field locations for PML, overlap region, and interior. Boxed velocities and potentials are used to transfer fields between the interior and the PML.

$$\bar{v} = \nabla\Phi + \nabla\times\bar{\Psi}$$
$$= \left(\frac{\partial\Phi}{\partial x} - \frac{\partial\Psi_y}{\partial z}\right)\hat{x} + \left(\frac{\partial\Phi}{\partial z} + \frac{\partial\Psi_y}{\partial x}\right)\hat{z}, \tag{1}$$

where Φ is the compressional potential and Ψ_y is the y component of the shear potential. For the two-dimensional problem, the vector nature of Ψ_y may be suppressed. However, to maintain consistency with future work on the three-dimensional problem, the subscript y is retained. Potentials are computed using

$$\frac{\partial^2\Phi}{\partial t^2} = c_p^2\left(\frac{\partial v_x}{\partial x} + \frac{\partial v_z}{\partial z}\right), \tag{2}$$

$$\frac{\partial^2\Psi_y}{\partial t^2} = c_s^2\left(\frac{\partial v_x}{\partial z} - \frac{\partial v_z}{\partial x}\right), \tag{3}$$

where $c_p = \sqrt{(\lambda+2\mu)/\rho}$ is the P-wave velocity, $c_s = \sqrt{\mu/\rho}$ is the S-wave velocity, λ and μ are Lamé constants, and ρ is the density. In Fig. 2, the potentials and velocities with boxed labels are computed using (1)–(3). The reader is referred to Ref. 16 for the finite-difference forms of these equations.

The potentials satisfy the following scalar wave equations:

$$\frac{\partial^2\Phi}{\partial t^2} = c_p^2\nabla^2\Phi, \tag{4}$$

$$\frac{\partial^2\Psi_y}{\partial t^2} = c_s^2\nabla^2\Psi_y. \tag{5}$$

To simulate these wave equations on a grid of the same form used for acoustic fields, they are each rewritten as a set of three coupled equations:

$$\frac{\partial\Phi}{\partial t} = (\lambda+2\mu)\left(\frac{\partial A_x}{\partial x} + \frac{\partial A_z}{\partial z}\right), \tag{6}$$

$$\frac{\partial A_x}{\partial t} = \frac{1}{\rho}\frac{\partial\Phi}{\partial x}, \tag{7}$$

$$\frac{\partial A_z}{\partial t} = \frac{1}{\rho}\frac{\partial\Phi}{\partial z}, \tag{8}$$

$$\frac{\partial\Psi_y}{\partial t} = \mu\left(\frac{\partial B_x}{\partial x} + \frac{\partial B_z}{\partial z}\right), \tag{9}$$

$$\frac{\partial B_x}{\partial t} = \frac{1}{\rho}\frac{\partial\Psi_y}{\partial x}, \tag{10}$$

$$\frac{\partial B_z}{\partial t} = \frac{1}{\rho}\frac{\partial\Psi_y}{\partial z}. \tag{11}$$

Equations (6)–(8) can be decoupled to obtain (4) and (9)–(11) to obtain (5). The new fields $\bar{A}$ and $\bar{B}$ are introduced as part of a field-dividing process, and they are analogous to velocity in the acoustic equations. Figure 3(a) and (b) shows the spatial stencils for the equations governing potentials Φ and Ψ_y, respectively. Each stencil corresponds to a separate grid: One carries energy from the compressional wave and the other carries energy from the shear wave. These grids are

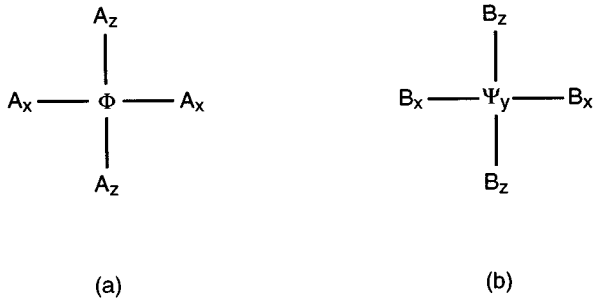

FIG. 3. Stencils for overlapping grids in the PML: (a) Stencil for the compressional potential. (b) Stencil for the shear potential.

overlayed in Fig. 2 so they can be viewed simultaneously. The ordered pair notation indicates that two field values exist at the same location. For example, the pairing ''A_z, B_x'' indicates that fields A_z and B_x share the same location, but are not related otherwise. Φ and Ψ_y grid points are shifted with respect to each other to satisfy the finite-difference forms of (1)–(3). In Appendix A it is shown that energy is propagated from the grid interior (including S-wave energy) via longitudinal waves.

Equations (6)–(11) describe the propagation of energy through the PML without loss. To eliminate reflections, the fields must be attenuated. Following Berenger,[18] we modify the lossless equations by ''splitting'' the potentials and adding loss terms to get

$$\frac{\partial \Phi_x}{\partial t}+(\lambda+2\mu)q_{px}\Phi_x=(\lambda+2\mu)\,\frac{\partial A_x}{\partial x}, \tag{12}$$

$$\frac{\partial \Phi_z}{\partial t}+(\lambda+2\mu)q_{pz}\Phi_z=(\lambda+2\mu)\,\frac{\partial A_z}{\partial z}, \tag{13}$$

$$\frac{\partial A_x}{\partial t}+\frac{1}{\rho}\,q^*_{px}A_x=\frac{1}{\rho}\,\frac{\partial(\Phi_x+\Phi_z)}{\partial x}, \tag{14}$$

$$\frac{\partial A_z}{\partial t}+\frac{1}{\rho}\,q^*_{pz}A_z=\frac{1}{\rho}\,\frac{\partial(\Phi_x+\Phi_z)}{\partial z}, \tag{15}$$

$$\frac{\partial \Psi_{yx}}{\partial t}+\mu q_{sx}\Psi_{yx}=\mu\,\frac{\partial B_x}{\partial x}, \tag{16}$$

$$\frac{\partial \Psi_{yz}}{\partial t}+\mu q_{sz}\Psi_{yz}=\mu\,\frac{\partial B_z}{\partial z}, \tag{17}$$

$$\frac{\partial B_x}{\partial t}+\frac{1}{\rho}\,q^*_{sz}B_x=\frac{1}{\rho}\,\frac{\partial(\Psi_{yx}+\Psi_{yz})}{\partial x}, \tag{18}$$

$$\frac{\partial B_z}{\partial t}+\frac{1}{\rho}\,q^*_{sx}B_z=\frac{1}{\rho}\,\frac{\partial(\Psi_{yx}+\Psi_{yz})}{\partial z}. \tag{19}$$

The potentials are split such that $\Phi=\Phi_x+\Phi_z$ and $\Psi_y=\Psi_{yx}+\Psi_{yz}$. Equations (12)–(19) describe longitudinal waves that attenuate exponentially. For this work, exponential differencing was used as described in Ref. 18. However, it is possible and may be advantageous to use standard central differencing as discussed in Refs. 26 and 27.

The loss terms q_{ij} ($i=p, s$ and $j=x, z$) within the PML are proportional to $(r/\delta)^n$, where r is depth measured into the PML, δ is the total PML depth, and $n=4$ is empirically chosen for best performance and stability. Hence,

$$q_{ij}=q_{ij}^{\max}(r/\delta)^n. \tag{20}$$

The maximum loss values $q_{ij}^{\max}$ are set such that the reflection coefficient is a small but nonzero value. The reflection coefficients at normal incidence, computed in the same manner as in Ref. 18 (see Appendix B), are

$$R_{pp}=\exp\left(-\frac{2q^{\max}\delta(\lambda+2\mu)}{(n+1)c_p}\right), \tag{21}$$

$$R_{ss}=\exp\left(-\frac{2q^{\max}\delta\mu}{(n+1)c_s}\right), \tag{22}$$

where R_{pp} and R_{ss} are the reflection coefficients for P and S waves, respectively. These equations are correct provided that the starred loss terms are related to nonstarred terms through the matching conditions

$$(\lambda+2\mu)q=q^*/\rho, \tag{23}$$

$$\mu q=q^*/\rho. \tag{24}$$

Equations (21) and (22) can be solved for $q^{\max}$ once a maximum reflection coefficient has been chosen. Here we have used $R_{pp}=R_{ss}=10^{-6}$. As shown in Fig. 1, some loss terms are set to zero within the edge portions (as opposed to corners) of the PML. This preserves the phase-velocity tangential to the PML-interior interface and results in an impedance match between the PML and interior that is independent of the incident angle. Terms q_{ix} are zero for the top and bottom PML, while terms q_{iz} are zero for the left and right PML. This dictates that exponential decay occurs only in the direction perpendicular to the edge of the PML. In the corners, losses are nonzero in both directions, and the variation of loss with depth corresponds to that in the appropriate neighboring PML edge region. For potentials occurring in the overlap zone, either at or inside the edge of the PML, the standard finite-difference formulation (6)–(11) is used.

In a typical problem, there are three computational regions—the interior stress–velocity grid, the overlap region, and the PML. The following list explicitly outlines the sequence in which computations are performed (refer to Fig. 2):

(1) Stress values τ_{xx}, τ_{zz}, and τ_{xz} are computed throughout the interior and overlap regions using the stress–velocity equations.
(2) Potentials Φ and Ψ_y are computed in the overlap region using (2) and (3) for values with boxed labels and (6) and (9) for the remaining values.
(3) Potentials Φ_x, Φ_z, Ψ_{yx}, and Ψ_{yz} are computed in the PML using (12), (13), (16), and (17) with appropriate loss terms set to zero.
(4) The fields A_x, A_z, B_x, and B_z are computed in the PML using (14), (15), (18), and (19) with appropriate loss terms set to zero and in the overlap region using (7), (8), (10), and (11).

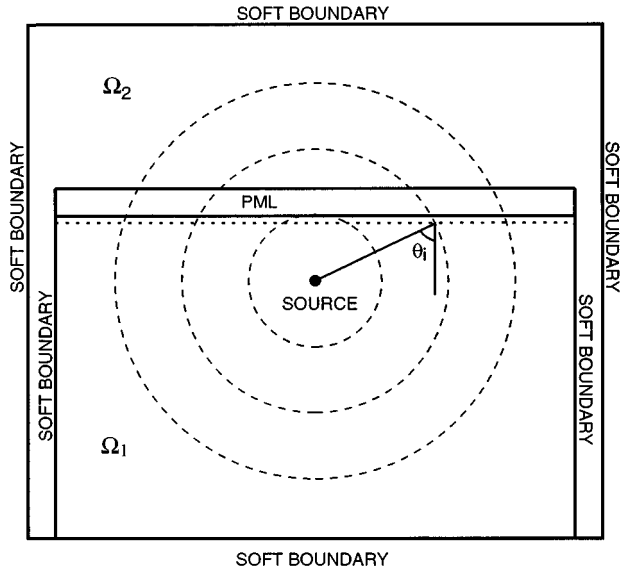

FIG. 4. Geometry for computing reflection factors. Domain Ω_1 is terminated on the upper edge with a PML. The dimensions are such that reflections are caused only by the ABC for the duration of the simulation. Domain Ω_2 is large enough so that no reflections occur.

(5) Velocities v_x and v_z are computed in the overlap region using (1) for values with boxed labels and using the stress–velocity equations in the interior.

II. NUMERICAL RESULTS

In this section reflection factors computed using numerical simulations are presented. Within the limits of the simulations, these factors are good indicators of the angular performance of an ABC. Figure 4 shows the test geometry, consisting of two distinct computational domains, Ω_1 and Ω_2, which are used to evaluate the ABC. Grid Ω_1 is terminated by a PML on the top and by soft boundaries on the other edges; grid Ω_2 is terminated with soft boundaries on all sides. As shown, Ω_2 models a larger area than Ω_1. A source is placed three wavelengths below the PML region in Ω_1 and at the corresponding location in Ω_2. Waves radiating away from the source in Ω_1 will intersect the lower edge of the overlap region at an incident angle θ_i. For waves radiating in Ω_2, no boundary is present at this location and the waves propagate without reflection. For all cw examples shown, we use 16 grid spaces per S-wave wavelength and, for stability, we use $c_p \delta t/\Delta = 0.707$ where δt is one time step and Δ is one spatial step. The material parameters correspond to basalt ($c_p = 5710$ m/s and $c_s = 2930$ m/s).

The reflection factors are defined as follows:

$$R_{pp} = \frac{\Phi_{\Omega_1} - \Phi_{\Omega_2}}{\Phi_{\Omega_2}}, \tag{25}$$

$$R_{ps} = \frac{\Psi_{y\Omega_1}}{\Phi_{\Omega_2}}, \tag{26}$$

$$R_{ss} = \frac{\Psi_{y\Omega_1} - \Psi_{y\Omega_2}}{\Psi_{y\Omega_2}}, \tag{27}$$

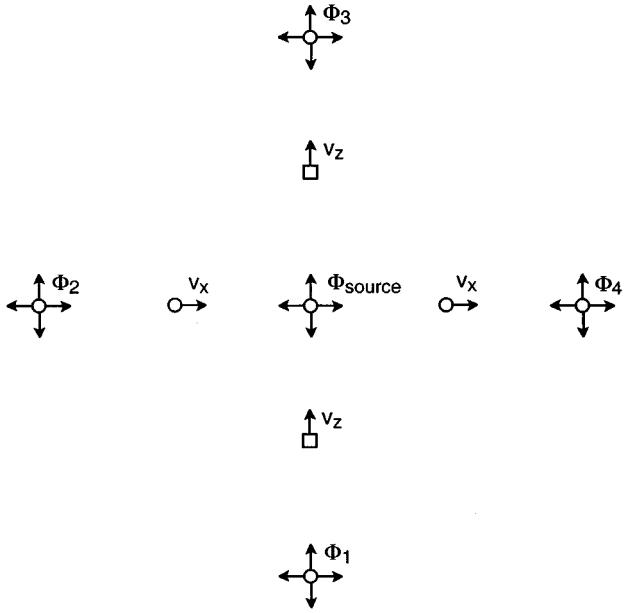

FIG. 5. Grid points used to implement P-wave source. Five potentials are computed from their neighboring velocities. The source function is added to Φ_{source}. The velocities are computed from neighboring potentials to couple the source field into the stress–velocity grid.

$$R_{sp} = \frac{\Phi_{\Omega_1}}{\Psi_{y\Omega_2}} \tag{28}$$

so that R_{pp} and R_{ps} measure the reflected P and S waves due to an incident P wave, and R_{ss} and R_{sp} measure the reflected S and P waves due to an incident S wave. The potentials are computed using (2) and (3) for both grids, and the data are averaged so that both potentials are collected at the same points, corresponding to the lower edge of the overlap region in Ω_1. The source excitation is harmonic; hence, the magnitude and phase of the potential may be computed as in Ref. 28.

Equations (25)–(28) impose two requirements on the test simulation. First, the grids must be large enough so that only reflections caused by the presence of the PML in Ω_1 are recorded, i.e., no reflections are recorded from the soft boundaries. Second, the incident field should be either a pure P wave to obtain R_{pp} and R_{ps} or a pure S wave to obtain R_{ss} and R_{sp}. Despite the first requirement, the grid size must be limited to one which is numerically tractable. In our examples, the grids are large enough to compute reflection factors for incident angles in the range $0° \leqslant \theta_i \leqslant 80°$. To satisfy the second requirement, four potentials are used in conjunction with the source potential Φ_{source}. Figure 5 shows the geometry of the P-wave source. The forcing function added to the source potential is given by

$$F_{cw}(l) = \Phi_0(1 - \exp(-\alpha l^2))\sin\left(\frac{(0.707)2\pi l c_s}{N_s c_p}\right), \tag{29}$$

where l indicates the current time step and N_s is the number of grid points per S-wave wavelength. The value 0.707 is chosen to insure stability.[29] The value of Φ_0 is chosen to give an upper bound of unity for the stress components, and the

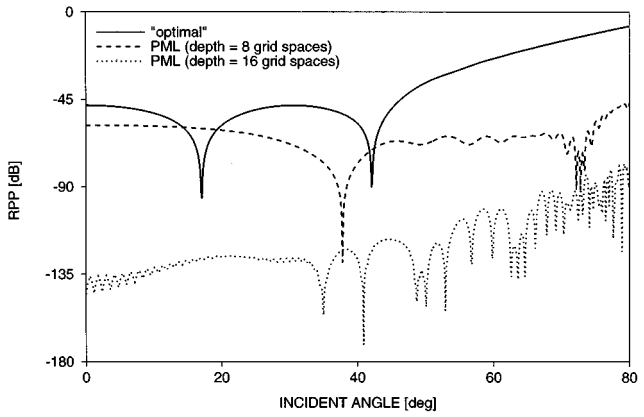

FIG. 6. Comparison of R_{pp} for the ''optimal'' and PML ABCs. The PML has depths $\delta=8\Delta$ and 16Δ. R_{ps} is negligible for both ABCs.

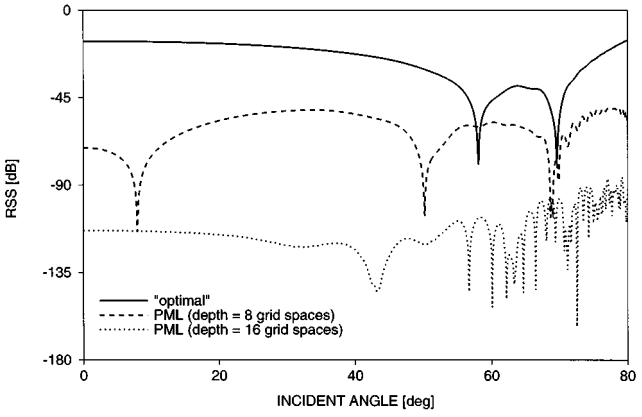

FIG. 7. Comparison of R_{ss} for the ''optimal'' and PML ABCs. The PML has depths $\delta=8\Delta$ and 16Δ. R_{sp} is negligible for both ABCs.

factor α is chosen so the source field reaches half its maximum amplitude at the end of one cycle. The surrounding potentials $\Phi_1-\Phi_4$ are computed using (2). The velocities v_x and v_z are computed from the five potentials using (1) with Ψ_y set to zero. The Ψ_y values that occur when the source is implemented in this way are smaller than the Φ values by a factor of 10^{-12}. The approach for computing the S-wave source is similar except that its location is shifted by a half-grid space and Φ is set to zero in (1). Note that to implement these sources, potentials are computed only around the source point rather than over the entire interior.

To examine the performance of the PML, comparisons with the second-order ABC of Peng and Toksöz are presented. The latter ABC has been shown to absorb better than the ABCs of Higdon[11] and Reynolds.[13] It is referred to as an ''optimal'' ABC because the poles and zeros of its numerically derived reflection coefficients have been forced into positions on the unit circle in the complex z-plane. Such a placement produces a stable ABC with optimal performance. The coefficients used to implement the ''optimal'' ABC can be optimized for either S- or P-wave absorption, but not both. For our comparisons, the optimal coefficients were chosen to have maximum absorption for P waves. The ''optimal'' ABC is applied to τ_{zz} and v_x nodes lying along the upper edge of the Ω_1 grid. An alternative approach is to apply the ABC to the v_x and v_z nodes, which is similar to the procedure presented in Ref. 15. However, for the material parameters used here, this scheme produces excessively large cross coupling terms, R_{ps} and R_{sp}. Although application of the ABC to τ_{zz} and v_x nodes does not produce the ''physical'' zero in R_{pp} and R_{ss}, the ABC so applied produces no cross coupling and, hence, is the preferred formulation.

Figures 6 and 7 show R_{pp} and R_{ss}, respectively, as functions of θ_i. In each case, the PML is compared to the ''optimal'' ABC. Results are shown for PML depths, δ, of 8 and 16 grid spaces. The ''optimal'' ABC is configured to give best absorption at angles $\theta_i=20°$ and 40° and, in both cases, the ABC is optimized for P-wave absorption. Figure 6 shows that the ''optimal'' ABC performs well for P-wave illumination with nulls occurring approximately at the expected angles. For $\delta=16\Delta$, the PML has substantially lower reflection levels over the angles shown. For $\delta=8$, the performance has degraded, but R_{pp} remains below 1% for all angles. Figure 7 shows that the ''optimal'' ABC performance degrades for S-wave illumination, while the PML performance remains unaffected. The coupling of energy between S and P waves is measured by the reflection factors R_{ps} and R_{sp}. These factors were below -200 dB over all incident angles for both the PML and the ''optimal'' ABC.

Figure 8 shows the test geometry for comparing the ''optimal'' and PML ABCs for transient illumination. The source is positioned at the center of a $400\Delta\times150\Delta$ subregion of the grid indicated by the dash-dot box. The grid is terminated by soft boundaries on the left and right edges and by the PML ($\delta=16\Delta$) and ''optimal'' ABCs on the top and bottom edges, respectively. Figure 9 shows a series of snapshots of the boxed region. Figure 9(a) and (b) shows the compressional potential at two successive times for a pure P-wave source. The forcing function added to the source potential is a delayed Ricker wavelet

$$F_{\text{pulse}}(l)=(1-2\pi^2 p(l)^2)e^{-\pi^2 p(l)^2}, \tag{30}$$

with

$$p(l)=\left(\frac{c_s(0.707)}{c_p N_s}\right)\left(l-\frac{c_p N_s}{c_s(0.707)}\right), \tag{31}$$

where, as before, l is an integer indicating the current time step. In this context, N_s is the number of points per shear wavelength at the frequency with maximum spectral energy. A logarithmic scaling of the amplitudes has been used to enhance small reflections. A visible reflection occurs at the lower edge for the ''optimal'' ABC, while the PML shows no reflection. For a pure S-wave source, the shear potential is

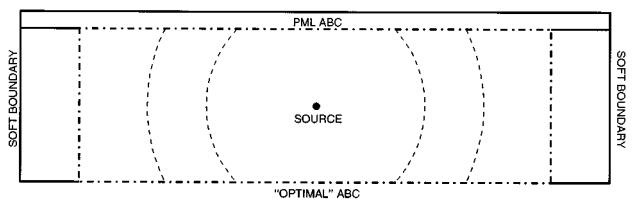

FIG. 8. Geometry for comparing ''optimal'' and PML ABCs under transient illumination. The dash-dot box indicates the area shown in the snapshots. It has dimensions $400\Delta\times150\Delta$.

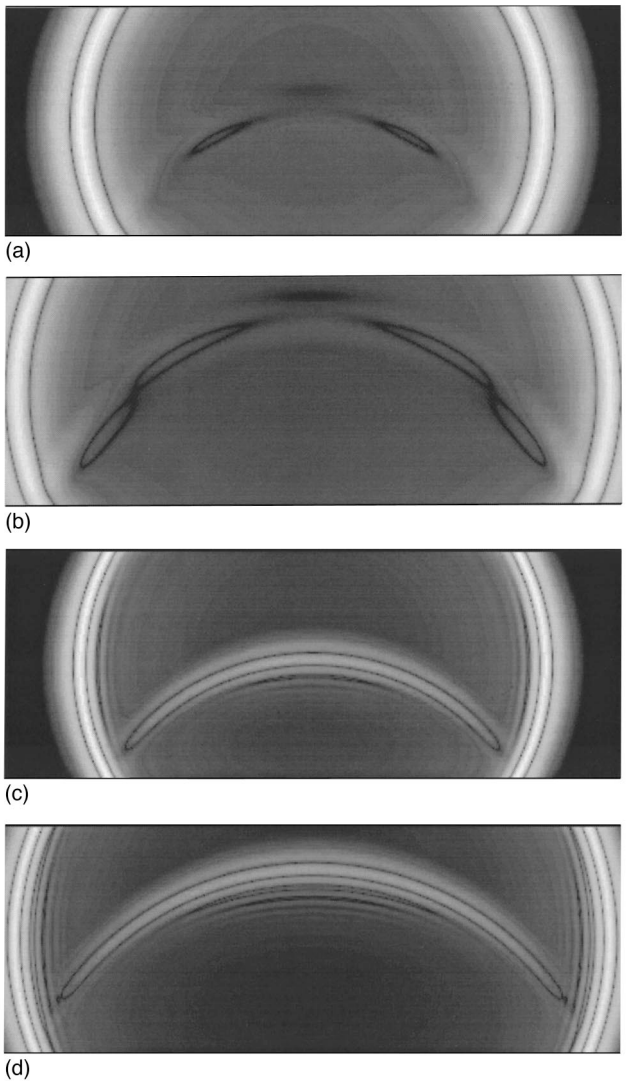

FIG. 9. Comparison of the PML ABC with the ''optimal'' ABC. Snapshots of potentials are shown at two separate times after the incident wave has reached both ABCs. Compressional potentials are shown for an incident *P* wave in (a) and (b), and shear potentials are shown for an incident *S* wave in (c) and (d).

shown in Fig. 9(c) and (d). Since the ''optimal'' ABC was not optimized for *S*-wave absorption, the reflections are much larger. However, once again, no reflections are evident at the PML boundary.

In both the interior and PML portions of the computational domain, the number of computations per time step is proportional to the number of unknowns. Within the two-dimensional PML an additional three unknowns per grid cell are required. For large-scale problems, the PML represents only a small portion of the total grid area and, hence, the increase in the number of computations is modest. However, the overall computational cost for many problems can be lower because the superior quality of the PML allows the ABC to more tightly bound the region of interest. In addition, the thickness of the PML can be reduced depending on the dynamic range requirements of the problem.

To verify stability experimentally, an interior region was completely enclosed by a PML, as shown in Fig. 1. For each type of source, a simulation was run for 3000 cycles of the incident field, and the corresponding potentials were examined. No artificial reflections were evident.

The use of potentials in the implementation of the PML prohibits its use in regions where shear and compressional waves are coupled (such as at media interfaces). Hence, it cannot be applied where a media interface will intersect the PML. It can be applied directly to problems with discrete scatterers present in an otherwise homogeneous medium. To model multilayer scattering, a second ABC (such as the ''optimal'' ABC) can be used in conjunction with the PML. The PML would be applied on computational boundaries parallel to the media interfaces, while the second ABC would be used on the remaining boundaries.

III. SUMMARY

We have adapted the PML ABC for use with elastic materials. Our technique allows successful transfer of wave energy from a velocity–stress grid to a set of two grids, one for shear waves and one for compressional waves, in which the energy exponentially decays. The resulting formulation was tested numerically through the computation of reflection factors and snapshots of the potentials. These tests indicate that the PML is superior to the ''optimal'' ABC for both broadband and wide angle performance. The PML is best suited for modeling discrete scatterers but, in conjunction with another ABC, it can also be applied to multilayer problems. Stability was confirmed experimentally. The extension of this method to three dimensions is straightforward and is the subject of future work.

ACKNOWLEDGMENTS

This work was supported by the Office of Naval Research, Code 321OA and by the National Science Foundation under Grant No. ECS9253547.

APPENDIX A: CONVERSION BETWEEN VELOCITY AND POTENTIAL

Potentials Φ and Ψ_y are related to fields $\bar{A}$ and $\bar{B}$ through (6)–(11) in a similar manner as pressure is related to velocity in the acoustic equations. These equations were chosen because they satisfy the scalar wave equation, and their structure can be modified to obtain the form of the PML equations given in Ref. 18. Other formulations may be possible, but an exhaustive survey is beyond the scope of this paper.

Equations (6)–(11) support the propagation of two longitudinal waves which have both $\bar{A}$ and $\bar{B}$ oriented in the direction of propagation. To show that the shear and compressional components of the velocity are transformed to the appropriate potential waves with the correct orientation, consider the field

$$\bar{v}=\bar{v}_s+\bar{v}_p, \tag{A1}$$

where $\bar{v}_s$ and $\bar{v}_p$ are velocities due to the shear and compressional waves (see Fig. A1),

$$\bar{v}_p=\tilde{v}_{0p}(\cos\ \xi\hat{x}+\sin\ \xi\hat{z}), \tag{A2}$$

$$\bar{v}_s=\tilde{v}_{0s}(-\sin\ \eta\hat{x}+\cos\ \eta\hat{z}), \tag{A3}$$

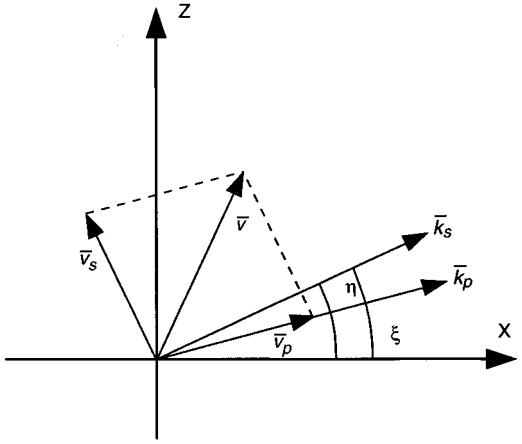

FIG. A1. Geometry of wave propagating in the grid interior.

with

$$\tilde{v}_{0p}=v_{0p}e^{j(\omega t-k_{xp}x-k_{zp}z)} \tag{A4}$$

$$\tilde{v}_{0s}=v_{0s}\ e^{\ j(\omega t-k_{xs}x-k_{zs}z)}, \tag{A5}$$

where $k_{xs}=k_s\cos\eta$, $k_{zs}=k_s\sin\eta$, $k_{xp}=k_p\cos\xi$, $k_{zp}=k_p\sin\xi$, and k_p and k_s are the wave numbers for the compressional and shear waves, respectively. Angles ξ and η are measured from the positive x axis, and ω is the radian frequency. The components of the total velocity are

$$v_x=v_{xp}+v_{xs}=\tilde{v}_{0p}\cos\xi-\tilde{v}_{0s}\sin\eta, \tag{A6}$$

$$v_z=v_{zp}+v_{zs}=\tilde{v}_{0p}\sin\xi+\tilde{v}_{0s}\cos\eta. \tag{A7}$$

To verify that the orientation of the potential fields is as expected, this superposition of waves will be transformed into the fields $\bar{A}$ and $\bar{B}$. Using (A6) and (A7) in (2) and (3) yields, after some simplification,

$$\Phi=j\frac{k_pc_p^2\tilde{v}_{0p}}{\omega^2}, \tag{A8}$$

$$\Psi_y=-j\frac{k_sc_s^2\tilde{v}_{0s}}{\omega^2}, \tag{A9}$$

which can be used in (7), (8), (10), and (11) to obtain expressions for $\bar{A}$ and $\bar{B}$

$$\bar{A}=-j\frac{k_p^2c_p^2\tilde{v}_{0p}}{\rho\omega^3}(\cos\xi\hat{x}+\sin\xi\hat{z}), \tag{A10}$$

$$\bar{B}=j\frac{k_s^2c_s^2\tilde{v}_{0s}}{\rho\omega^3}(\cos\eta\hat{x}+\sin\eta\hat{z}). \tag{A11}$$

Equations (A10) and (A11) show that $\bar{A}$ and $\bar{B}$ are longitudinal waves with $\bar{A}$ oriented in the direction of propagation of the compressional wave and $\bar{B}$ oriented in the direction of propagation of the shear wave. Furthermore, $\bar{A}$ is related to the compressional wave $\tilde{v}_{0p}$ and $\bar{B}$ is related to the shear wave $\tilde{v}_{0s}$. It can be shown that this relationship also holds for the transformation of $\bar{A}$ and $\bar{B}$ to velocity. This is done by substituting (A10) and (A11) into (6) and (9), respectively, and then using the resulting potentials in (1).

APPENDIX B: MATCHING CONDITIONS

The PML equations, (12)–(19), are designed to support propagation of a plane wave that decays exponentially in the direction normal to the interface. Unlike the lossless equations, (6)–(11), they cannot be decoupled to produce the wave equations, (4) and (5). However, the phase velocity tangential to the PML is equivalent to that supported by the lossless equations and is independent of incident angle. This insures that reflections will not occur at the interface between the interior region and the PML.

To derive the reflection coefficient (21) and the matching condition (23), consider a longitudinal wave of the form

$$A_x=A_0\cos\xi e^{j(\omega t-k_xx-k_zz)}, \tag{B1}$$

$$A_z=A_0\sin\xi e^{j(\omega t-k_xx-k_zz)}, \tag{B2}$$

$$\Phi_x=\Phi_{0x}e^{j(\omega t-k_xx-k_zz)}, \tag{B3}$$

$$\Phi_z=\Phi_{0z}e^{j(\omega t-k_xx-k_zz)}, \tag{B4}$$

where $\bar{A}=(A_x,A_z)$ is oriented in the same direction as $\bar{v}_p$ in Fig. A1, and $\Phi=\Phi_x+\Phi_z$ is a scalar field. In this Appendix, k (without subscript) is used to represent the compressional wave number. Assuming A_0 is specified, the unknowns are k_x, k_z, Φ_{0x}, and Φ_{0z}. Substituting (B1)–(B4) into (12)–(15) yields

$$\Phi_{0x}\left(1-j\frac{(\lambda+2\mu)q_{px}}{\omega}\right)=-\frac{(\lambda+2\mu)k_xA_0\cos\xi}{\omega}, \tag{B5}$$

$$\Phi_{0z}\left(1-j\frac{(\lambda+2\mu)q_{pz}}{\omega}\right)=-\frac{(\lambda+2\mu)k_zA_0\sin\xi}{\omega}, \tag{B6}$$

$$A_0\cos\xi\left(1-j\frac{q_{px}^*}{\rho\omega}\right)=-\frac{k_x(\Phi_{0x}+\Phi_{0z})}{\rho\omega}, \tag{B7}$$

$$A_0\sin\xi\left(1-j\frac{q_{pz}^*}{\rho\omega}\right)=-\frac{k_z(\Phi_{0x}+\Phi_{0z})}{\rho\omega}. \tag{B8}$$

Φ_{0x} and Φ_{0z} are found from (B5) and (B6) and substituted into (B7) and (B8) to obtain

$$\frac{\omega^2}{c_p^2}\cos\xi\left(1-j\frac{q_{px}^*}{\rho\omega}\right)=k_x\left(\frac{k_x\cos\xi}{1-j\dfrac{(\lambda+2\mu)q_{px}}{\omega}}+\frac{k_z\sin\xi}{1-j\dfrac{(\lambda+2\mu)q_{pz}}{\omega}}\right), \tag{B9}$$

$$\frac{\omega^2}{c_p^2}\sin\xi\left(1-j\frac{q_{pz}^*}{\rho\omega}\right)=k_z\left(\frac{k_x\cos\xi}{1-j\dfrac{(\lambda+2\mu)q_{px}}{\omega}}+\frac{k_z\sin\xi}{1-j\dfrac{(\lambda+2\mu)q_{pz}}{\omega}}\right). \tag{B10}$$

Taking the ratio of (B10) and (B9) yields

$$\frac{k_z}{k_x}=\frac{\sin\ \xi}{\cos\ \xi}\frac{1-j(q^*_{pz}/\rho\omega)}{1-j(q^*_{px}/\rho\omega)}. \tag{B11}$$

To obtain k_z^2, (B11) is solved for k_x which is substituted into (B10). To obtain k_x^2, (B11) is solved for k_z which is substituted into (B9). Taking the positive square roots for the forward traveling wave yields

$$k_x=\frac{\omega\ \cos\ \xi[1-j(q^*_{px}/\rho\omega)]}{c_pG}, \tag{B12}$$

$$k_z=\frac{\omega\ \sin\ \xi[1-j(q^*_{pz}/\rho\omega)]}{c_pG}, \tag{B13}$$

where

$$G=\sqrt{W_x\ \cos^2\ \xi+W_z\ \sin^2\ \xi}, \tag{B14}$$

$$W_x=\frac{1-j(q^*_{px}/\rho\omega)}{1-j[(\lambda+2\mu)q_{px}/\omega]}, \tag{B15}$$

$$W_z=\frac{1-j(q^*_{pz}/\rho\omega)}{1-j[(\lambda+2\mu)q_{pz}/\omega]}. \tag{B16}$$

A special case occurs when matching condition (23) holds, namely the quantities W_x, W_z, and G become unity. For this condition, (B12) and (B13) are substituted into (B1)–(B4) to obtain waves of the general form

$$\zeta=\zeta_0 e^{j(\omega t-k_{xr}x-k_{zr}z)}e^{k_{xi}x}e^{k_{zi}z}, \tag{B17}$$

where ζ may be replaced by A_x, A_z, Φ_x, or Φ_z. The real and imaginary parts of k_x and k_z are

$$k_{xr}=\frac{\omega\ \cos\ \xi}{c_p}, \tag{B18}$$

$$k_{xi}=-\frac{q^*_{px}\ \cos\ \xi}{\rho c_p}, \tag{B19}$$

$$k_{zr}=\frac{\omega\ \sin\ \xi}{c_p}, \tag{B20}$$

$$k_{zi}=-\frac{q^*_{pz}\ \sin\ \xi}{\rho c_p}. \tag{B21}$$

Equations (B17)–(B21) show that exponential attenuation occurs in the direction perpendicular to the edge of the PML when the appropriate loss term is set to zero (see Fig. 1).

A wave traveling in the PML will be attenuated until it is reflected at a boundary. The reflected wave will undergo further attenuation until it reaches the overlap region. For a PML of thickness δ, this process results in the reflection coefficient

$$R_{pp}=\exp\left\{-\frac{2(\lambda+2\mu)\delta}{c_p}\int_0^\delta q(r)\ dr\right\}, \tag{B22}$$

where matching condition (23) has been used to eliminate the starred loss term and $q(r)$ represents either q_{px} or q_{pz}. The loss term is a function of position within the PML as given by (20). Hence, when the integral is evaluated in (B22), the result is (21). Repeating the steps above for the Ψ_y and $\bar{B}$ fields using (17)–(19) results in the matching condition (24) and the reflecton coefficient (22).

[1] A. R. Levander, ''Use of the telegraphy equation to improve absorbing boundary efficiency for fourth-order acoustic wave finite difference schemes,'' Bull. Seismol. Soc. Am. **75**(6), 1847–1852 (1985).

[2] C. Cerjan, D. Kosloff, R. Kosloff, and M. Reshef, ''A nonreflecting boundary condition for discrete acoustic and elastic wave equations,'' Geophysics **50**(4), 705–708 (1985).

[3] M. E. Dougherty and R. A. Stephen, ''Seismic energy partitioning and scattering in laterally heterogeneous ocean crust,'' Pure Appl. Geophys. **128**(1/2), 195–229 (1988).

[4] A. R. Levander, ''Fourth-order finite-difference *P-SV* seismograms,'' Geophysics **53**(11), 1425–1436 (1988).

[5] R. A. Stephen, ''A review of finite difference methods for seismo-acoustics: Problems at the seafloor,'' Rev. Geophys. **26**(3), 445–458 (1988).

[6] R. A. Stephen and S. A. Swift, ''Finite difference modeling of geoacoustic interaction at anelastic seafloors,'' J. Acoust. Soc. Am. **95**, 60–70 (1994).

[7] R. A. Stephen and S. A. Swift, ''Modeling seafloor geoacoustic interaction with a numerical scattering chamber,'' J. Acoust. Soc. Am. **96**, 973–990 (1994).

[8] R. Clayton and B. Engquist, ''Absorbing boundary conditions for acoustic and elastic wave equations,'' Bull. Seismol. Soc. Am. **67**(6), 1529–1539 (1977).

[9] R. L. Higdon, ''Absorbing boundary conditions for difference approximations to the multi-dimensional wave equation,'' Math. Comput. **47**(176), 437–459 (1986).

[10] R. L. Higdon, ''Numerical absorbing boundary conditions for the wave equation,'' Math. Comput. **49**(179), 65–90 (1987).

[11] R. L. Higdon, ''Absorbing boundary conditions for elastic waves,'' Geophysics **56**(2), 231–241 (1991).

[12] L. T. Long and J. S. Liow, ''A transparent boundary for finite-difference wave simulation,'' Geophysics **55**(2), 201–208 (1990).

[13] A. C. Reynolds, ''Boundary conditions for the numerical solution of wave propagation problems,'' Geophysics **43**(6), 1099–1110 (1978).

[14] Z. P. Liao, H. L. Wong, B.-P. Yang, and Y.-F. Yuan, ''A transmitting boundary for transient wave analysis,'' Sci. Sin., Ser. A **27**(10), 1063–1076 (1984).

[15] C. Peng and M. N. Toksöz, ''An optimal absorbing boundary condition for finite difference modeling of acoustic and elastic wave propagation,'' J. Acoust. Soc. Am. **95**, 733–745 (1994).

[16] C. J. Randall, ''Absorbing boundary for the elastic wave equation: Velocity–stress formulation,'' Geophysics **54**(9), 1141–1152 (1989).

[17] E. L. Lindman, '' 'Free-space' boundary conditions for the time dependent wave equation,'' J. Comput. Phys. **18**, 66–78 (1975).

[18] J.-P. Berenger, ''A perfectly matched layer for the absorption of electromagnetics waves,'' J. Comput. Phys. **114**, 185–200 (1994).

[19] W. C. Chew, W. H. Weedon, and A. Sezginer, ''A 3-D perfectly matched medium by coordinate stretching and its absorption of static fields,'' in *11th Annual Review of Progress in Applied Computational Electromagnetics,* Monterey, CA, 1995, Vol. 1, pp. 482–489.

[20] W. C. Chew and W. H. Weedon, ''A 3D perfectly matched medium from modified Maxwell's equations with stretched coordinates,'' Microwave Opt. Technol. Lett. **7**(13), 599–604 (1994).

[21] Since this paper was accepted for publication, Chew and Liu have formulated an elastic PML from stretched coordinates that does not require the use of potentials. See *Proceedings of the IEEE Antennas and Propagation Society International Symposium* (IEEE, New York, 1996), Vol. 1, pp. 366–369.

[22] R. Mittra and Ü. Pekel, ''A new look at the perfectly matched layer (PML) concept for the reflectionless absorption of electromagnetic waves,'' IEEE Microwave Guided Wave Lett. **5**(3), 84–86 (1995).

[23] C. E. Reuter, R. M. Joseph, E. T. Thiele, D. S. Katz, and A. Taflove, ''Ultrawideband absorbing boundary condition for termination of waveguiding structures in FD–TD simulations,'' IEEE Microwave Guided Wave Lett. **4**(10), 344–346 (1994).

[24] J. G. Maloney and K. E. Cummings, ''Adaptation of FDTD techniques to acoustic modeling,'' in *11th Annual Review of Progress in Applied Computational Electromagnetics*, Monterey, CA, 1995, Vol. 2, pp. 724–731.

[25] J. Virieux, ''*P-SV* wave propagation in heterogeneous media: Velocity-stress finite difference method,'' Geophysics **51**(4), 889–901 (1986).

[26] Z. Wu and J. Fang, ''Performance of the perfectly matched layer in modeling wave propagation in microwave and digital circuit interconnects,'' in

11th Annual Review of Progress in Applied Computational Electromagnetics, Monterey, CA, 1995, Vol. 1, pp. 504–511.
[27] P. G. Petropoulos, ''Analysis of exponential time differencing for FD–TD in highly conducting dielectrics,'' submitted to IEEE Trans. Antennas Propagat. (1996).
[28] F. D. Hastings, J. B. Schneider, and S. L. Broschat, ''A Monte-Carlo FDTD technique for rough surface scattering,'' IEEE Trans. Antennas Propag. **43**(11), 1183–1191 (1995).
[29] R. Courant, K. O. Friedrichs, and H. Lewy, ''On the partial difference equations of mathematical physics,'' Technical Report NYO-7689, New York University, Courant Institute of Mathematics, 1956, translated by P. Fox.